Applied Catalysis B: Environmental 184 (2016) 299–308

Contents lists available at ScienceDirect

Applied Catalysis B: Environmental

journal homepage: www.elsevier.com/locate/apcatb

Highly active subnano Rh/Fe(OH)$_x$ catalyst for preferential oxidation of CO in H_2-rich stream

Hongling Guan[a,b], Jian Lin[a], Lin Li[a], Xiaodong Wang[a,*], Tao Zhang[a]

[a] State Key Laboratory of Catalysis, Dalian Institute of Chemical Physics, Chinese Academy of Sciences, Dalian 116023, China
[b] University of Chinese Academy of Sciences, Beijing 100049, China

ARTICLE INFO

Article history:
Received 17 August 2015
Received in revised form
16 November 2015
Accepted 25 November 2015
Available online 27 November 2015

Keywords:
Rhodium
Fe(OH)$_x$
CO
Preferential oxidation
H_2

ABSTRACT

A novel catalyst formulation of 3.1 wt.% Rh/Fe(OH)$_x$ was prepared via a co-precipitation method and investigated for CO preferential oxidation in H_2-rich stream. This catalyst exhibited a wider temperature range of 20–70 °C for CO total removal and better resistance to CO_2 and H_2O compared with the standard gold catalyst, standing out as the best Rh-based catalyst ever. The Rh species were highly dispersed in a subnano scale of ~1 nm and improved the reducibility of Fe(OH)$_x$ support. The adsorption of O_2 was thus promoted over the reduced support, together with the weakened CO adsorption over the Rh clusters, permitting a non-competitive Langmuir–Hinshelwood mechanism through the elementary reaction of $CO_{(ad)} + O_{(ad)}$. The reaction rate equation of $r = k[CO]^{0.73}[O_2]^{0.64}$ and small apparent activation energy of 24 kJ mol^{-1} were then derived from the kinetic studies.

1. Introduction

The preferential oxidation of CO in H_2-rich stream (PROX) (Eqs. (1) and (2)) has been considered as the most promising approach to eliminate CO from the hydrogen resource for proton-exchange membrane fuel cells (PEMFCs) [1–3]. The prerequisite for an efficient PROX catalyst is sufficiently high activity in the low-temperature oxidation of CO, even the selectively total removal of CO. Non-precious catalysts, especially the CuO/CeO_2, have attracted considerable interest from economical point of view with exceptional selectivity and stability [4–9]. It is now well recognized that the performances are related to the redox behavior with the interfacial interaction, and modifications such as the addition of heteroatoms are studied to improve their efficiency and stability [10]. Improvements are also observed with proper geometric type of the interacting surfaces [11] or the catalysts composition and morphology [12] are carried out to improve their efficiency and stability, but the total CO conversion temperatures are generally higher than 100 °C. Supported gold catalysts are well-known for their superior activity in room-temperature CO oxidation [13], while few of them are appropriate for the PROX reaction due to the competitive oxidation of H_2 at elevated temperatures, especially in the presence of H_2O and CO_2 [14–16]. Among various catalysts developed, platinum group metal (PGM) based ones are the most intensively investigated and have been regarded as promising candidates, but the relatively high reaction temperatures (usually above 100 °C) seriously restrict their practical applications. In fact, due to the well-recognized significance of total CO removal at ambient temperatures for PEMFCs applications in transportation [3], endeavor efforts have been devoted to the design of highly active PROX catalysts, which still remains a formidable challenge.

$$CO + \frac{1}{2}O_2 \rightarrow CO_2 \quad \Delta H^{\circ}_{298} = -283.6 \text{ kJ mol}^{-1} \tag{1}$$

$$H_2 + \frac{1}{2}O_2 \rightarrow H_2O \quad \Delta H^{\circ}_{298} = -243.5 \text{ kJ mol}^{-1} \tag{2}$$

Rhodium is one of the most widely used PGMs, especially for the mitigation of automotive exhaust pollutants [17–20]. The oxidation of CO by O_2, as an important constituent for that mitigation and a typical probe reaction in heterogeneous catalysis [21], has been extensively studied over various Rh-containing samples including single crystals [22,23], model nanoparticles [24,25], and supported catalysts [26–28]. Nevertheless, most of the studies were conducted under high temperature and vacuum conditions while less attention was paid to the low temperature regions. Particularly rare investigations have been performed for PROX reaction. In fact, there is no claiming for total CO removal at ambient temperature over Rh-based catalysts so far. Previous kinetic and mechanism studies of CO oxidation over Rh-based single crystals and Al_2O_3 or SiO_2 supported catalysts advocated a Langmuir–Hinshelwood

* Corresponding author. Fax: + 86 411 84685940.
E-mail address: xdwang@dicp.ac.cn (X. Wang).

http://dx.doi.org/10.1016/j.apcatb.2015.11.040
0926-3373/

(L–H) mechanism, of which the CO inhibition of the O_2 activation was recognized as the inherent reasons for the poor reactivity at low temperatures [22,29]. Accordingly, the weakening of CO adsorption and/or the promotion of O_2 activation should be an effective method to design efficient Rh-based catalysts for the low-temperature CO oxidation and PROX reaction.

Up to now, various PGM catalyst formulations for PROX have been developed in terms of promoting the activity of low-temperature CO oxidation. The Fe-containing materials, one of the most widely used reducible oxides, have been intensively studied as promoters for PROX since the seminal work of Korotkikh and Farrauto [1,30]. Siani et al. suggested that the electronic interaction between Pt and Fe weakened the adsorption of CO on Pt, which in turn enhanced the rate of CO oxidation over $PtFe/SiO_2$ catalysts [31]. Kotobuki et al. ascribed the enhanced activity to the FeO_x species which strongly interacted with Pt and provided additional sites for O_2 adsorption over PtFe/mordenite catalyst [32]. Our group developed a promoted catalyst of $IrFe/Al_2O_3$ for PROX and proposed a bifunctional mechanism where the oxidation of CO occurred between CO on Ir sites and O_2 on FeO_x sites [33]. When we applied iron oxide directly as catalyst support, total CO conversion was realized at room temperature [34,35]. Similarly, Fu et al. accounted the superior PROX reactivity over $FeO_x/Pt/SiO_2$ catalyst for the interface-confined Fe^{2+} centers which not only weakened the CO adsorption but also facilitated the activation of O_2 [36]. Recently, with the results of DFT calculations and in situ DRIFTS experiments, Qiao et al. suggested that the weakened CO adsorption over Pt/FeO_x catalyst promoted the competitive adsorption of O_2, permitting mixture mechanisms of competitive and non-competitive/redox [37–39]. All the above cases highlighted the paramount role of O_2 activation and presented quotable reference for the fabrication of novel Rh-based catalyst for the efficient removal of CO. In this work, subnano Rh clusters were successfully prepared via a co-precipitation method with $Fe(OH)_x$ as support. The derived $Rh/Fe(OH)_x$ catalyst exhibited unprecedentedly high activity for PROX reaction with 100% CO conversion at a wide temperature range of 20–70 °C and good resistance to H_2O and CO_2. To our knowledge, it is the best Rh-based catalyst for PROX reported so far and even comparable with the standard gold catalyst. Detailed structure characterizations together with adsorption experiments and kinetic studies were conducted, with the traditional Rh/Al_2O_3 catalyst as comparison, to reveal the origin of its superior activity in the low temperature oxidation of CO.

2. Experimental

2.1. Catalyst preparation

$Rh/Fe(OH)_x$ catalyst was prepared by co-precipitation method at a water-bath of 80 °C. In detail, an aqueous mixture of $Fe(NO_3)_3{\cdot}9H_2O$ (1 M) and $RhCl_3{\cdot}3H_2O$ (0.1 M) was added dropwise to a 0.2 M NaOH solution under stirring at 80 °C. The final PH was controlled around 8.5. After stirring reaction for 3 h and still ageing for 1 h, the mixture was filtered and washed with hot deionized water several times to remove salts, chloride and nitrate ions. Then the catalyst was dried overnight at 80 °C. $Rh/Fe(OH)_x$ catalyst with nominal Rh loadings of 3.0 wt.% and 1.5 wt.% together with 3.0 wt.% Rh/Al_2O_3 catalyst were prepared with identical parameters. The actual loadings are 3.1 wt.%, 1.3 wt.% and 3.0 wt.%, respectively.

2.2. Activity test and kinetic studies

The catalytic activity was tested under atmospheric pressure in a fixed bed reactor with a U-shaped quartz tube of 10 mm inner diameter. Before evaluation, the $Rh/Fe(OH)_x$ and Rh/Al_2O_3 catalysts were subjected to a reduction pretreatment in a 20 mL min^{-1} flow of 10 vol.% H_2/He at 200 °C (temperature ramp at 10 °C min^{-1}) for 30 min. The 4.4 wt.% Au/Fe_2O_3 standard catalyst provided by the World Gold Council (Au/Fe_2O_3–WGC, further information of the standard catalyst can be found in Supplementary information) was also tested for comparison with pretreatment at 200 °C in pure He. The PROX activity was measured in flow of 40 vol.% H_2 + 1 vol.% CO + 1 vol.% O_2 (30 mL min^{-1}, WHSV: 18,000 mL h^{-1} g_{cat}^{-1}) and the catalyst bed was diluted with SiO_2. The effects of CO_2 (20 vol.%) and H_2O (3 or 10 vol.%) were also examined by bubbling the gas mixture through water at controlled temperatures. Stability tests were carried out at 80 °C with WHSV of 21,000 mL h^{-1} g_{cat}^{-1}. The gas lines were heated at 120 °C to avoid water condensation on the lines. The gas composition was monitored by an on-line gas chromatograph (Agilent 6890, TDX-01 column, TCD detector) using He as carrier gas. The detection limit for CO was 10 ppm.

CO conversion (X_{CO}) was calculated as (Eq. (3)):

$$X_{CO} = \frac{n_{CO}^{in} - n_{CO}^{out}}{n_{CO}^{in}} \times 100\% \quad (3)$$

Selectivity to CO_2 (S_{CO2}) was estimated from the oxygen mass balance as follows:

$$S_{CO_2} = \frac{n_{CO}^{in} - n_{CO}^{out}}{2\left(n_{O_2}^{in} - n_{O_2}^{out}\right)} \times 100\% \quad (4)$$

The oxygen excess factor (λ) is defined as Eq. (5) and the value used herein was 2:

$$\lambda = 2 \times \frac{n_{O_2}^{in}}{n_{CO}^{in}} \quad (5)$$

For kinetic measurements, the conversions of all reactants were maintained below 20% by conditioning the space velocity. The CO conversions (X_{CO}) were used to calculate the CO oxidation rates (mol_{CO} g_{Rh}^{-1} h^{-1}):

$$r_{CO} = \frac{X_{CO} \cdot N_{CO}}{m_{Rh}} \quad (6)$$

where m_{Rh} was the mass of rhodium in the reactor bed, N_{co} was CO molar gas flow rate in mol h^{-1}. The reaction rates could be converted into turnover frequencies (TOF):

$$TOF = \frac{r_{CO} \cdot M_{Rh}}{D_{Rh}} \quad (7)$$

where M_{Rh} was the molar weight of Rh and D_{Rh} was the dispersion of Rh.

$$k = Ae^{-Ea/RT} \quad (8)$$

$$r_{CO} = kP_{CO}^{\alpha_{CO}} P_{O_2}^{\alpha_{O_2}} \quad (9)$$

$$\ln r_{CO} = \alpha_{CO} \ln P_{CO} + \ln\left(k \times P_{O_2}^{\alpha_{O_2}}\right) \quad (10)$$

$$\ln r_{CO} = \alpha_{O_2} \ln P_{O_2} + \ln\left(k \times P_{CO}^{\alpha_{CO}}\right) \quad (11)$$

The apparent activation energies (Ea) and reaction orders can be determined according to the Arrhenius equation in Eq. (8) and power rate law in Eq. (9). The CO reaction orders α_{CO} were derived from in Eq. (10) by taking logarithm both sides of Eq. (5) with variant P_{CO} and constant P_{O2}. Similarly, O_2 reaction orders α_{O2} could be obtained under constant P_{CO} and variant P_{O2} from Eq. (11).

2.3. Catalyst characterization

The Rh loadings of the synthesized samples were determined using Thermo IRIS Interepid II inductively coupled plasma (ICP) (Thermo Electron Corporation). The sample was dissolved with nitrohydrochloric acid.

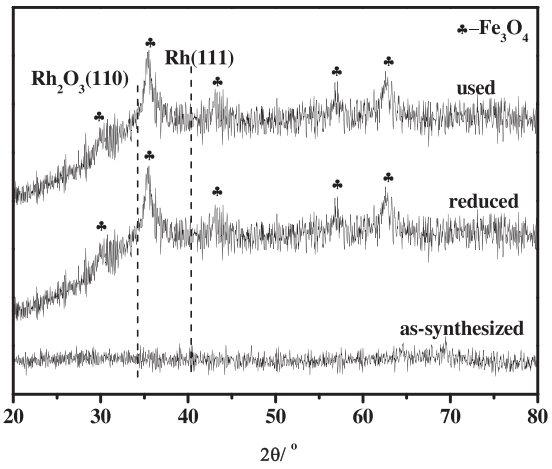

Fig. 1. XRD patterns of the as-synthesized, reduced and used Rh/Fe(OH)$_x$ samples.

The Brunauer–Emmett–Teller (BET) surface areas were measured by nitrogen adsorption at −196 °C using a Micromeritics ASAP 2010 apparatus. Before each measurement, the sample was evacuated at 120 °C to remove the adsorbents.

High resolution transmission electron microscopy (HR-TEM) observations were conducted on a JEOL (JEM-2100F) microscope. The samples were prereduced in 10 vol.% H_2/He at 200 °C. A few droplets of ultrasonically dispersed ethanol suspension of the reduced samples were deposited on a copper grid and dried in the air.

X-ray diffraction (XRD) experiments were carried out on a PW3040/60 X'Pert PRO (PANalytical) diffractometer equipped with a monochromatized Cu Kα radiation source (λ = 0.15432 nm), operating at 40 kV and 40 mA. A continuous mode was used for collecting data with a 2θ of 20–80° at a scanning speed of 10° min^{-1}.

The chemical states of Rh species in the samples were determined from X-ray photoelectron spectra (XPS) on a VGESCALAB 210 apparatus. Mg Kα radiation at an energy scale calibrated versus adventitious carbon (C_{1s} peak at 284.6 eV) was used. The samples were pretreated in 10 vol.% H_2/He at 200 °C for 30 min and purged with He for 1 h with cooling to room temperature. Then they were sealed in a glove box to ensure the air isolation. For measurements, the samples were transferred to the XPS chamber and detected at room temperature.

Auto Chem II 2920 was employed for H_2 temperature programmed reduction (H_2-TPR) experiment. A catalyst sample of ~100 mg was pretreated with Ar at 120 °C for 2 h to remove physically adsorbed water and surface carbonates. After cooling to 45 °C, the flow gas was switched to a flow of 10 vol.% H_2/Ar and the catalyst was heated to 900 °C at 10 °C/min. The consumption of H_2 was calculated with the H_2 peak area and calibration curve of the 10 vol.% H_2/Ar standard gas.

Adsorption microcalorimetry experiments of CO and O_2 were conducted with a BT 2.15 heat-flux calorimeter (Seteram, France). The calorimeter was connected to a volumetric system with MKS 698A Baratron Capacitance Manometers for precision pressure measurement ($\pm 1.33 \times 10^{-2}$ Pa). Prior to adsorption, the sample was reduced with H_2 at 200 °C for 30 min in a special treatment cell, and then cooled to room temperature followed by evacuation of 30 min. The adsorption experiment was conducted at 40 °C and the detailed procedures have been described previously [34].

IR spectra were collected in a diffuse reflectance (DRIFTS) mode using a Bruker EQUINOX 55 spectrometer, equipped with an MCT detector and operated at a resolution of 4 cm^{-1} for 64 scans. Before each experiment, the sample (~40 mg) was reduced in situ in 10 vol.% H_2/He at 200 °C in a DRIFTS cell (HC-500, Pike technologies). Then under flowing He, the temperature was cooled to 80 °C and hold for 30 min. After that, a background spectrum was recorded for the sample, which was then subtracted automatically from the subsequent spectra. The corresponding gas for CO adsorption (1 vol.% CO/He), CO oxidation reaction (1 vol.% CO + 1 vol.% O_2) and PROX reaction (1 vol.% CO + 1 vol.% O_2 + 40% vol. H_2) was introduced into the reaction cell consequently and the spectrum was recorded as a function of time until saturation. All the total flow rates involved were 20 mL min^{-1}.

3. Results

For clarity, the Rh loadings, BET surface areas and some other physicochemical properties are listed in Table 1. The Fe(OH)$_x$ and Al_2O_3 supported Rh catalysts possesses similar Rh loadings of around 3 wt.% and relatively high BET surfaces of 298 and 314 m^2 g^{-1}, respectively.

3.1. Structure characterizations

3.1.1. XRD and HR-TEM

Fig. 1 shows the XRD patterns of the as-synthesized, reduced, and used samples of Rh/Fe(OH)$_x$. The typical patterns of Fe_3O_4 in the reduced and used samples suggest the reduction of Fe(OH)$_x$ support, while the undetectable Rh-containing phases for all samples indicates the high dispersion of Rh species.

HR-TEM technique was further employed to visualize the morphologic structure of the reduced Rh/Fe(OH)$_x$ and Rh/Al_2O_3 samples. As shown in Fig. 2a and b, lattice fringes with a spacing of 0.242 nm corresponding to the (2 2 2) plane of Fe_3O_4 are clearly observed. The presence of Fe_3O_4 phases in the reduced Rh/Fe(OH)$_x$ samples confirms the reduction of Fe(OH)$_x$ support. Meanwhile, the majority of Rh species exist as clusters smaller than 1 nm. There are no Rh species larger than 2 nm by examining various regions at different magnifications. In comparison, the Rh species are dispersed in a scale of around 2 nm for the Rh/Al_2O_3 samples (Fig. 2c and d). These results indicate that the Fe(OH)*x* support plays an important role in dispersing and stabilizing the subnano Rh clusters, probably related to the defect sites of the partial reduced support [38].

3.1.2. H_2-TPR and XPS

Both the XRD and HR-TEM results suggest the reduction of Fe^{3+} at a relatively mild condition. H_2-TPR experiments were consequently conducted to detect the reducibility of Rh/Fe(OH)$_x$, with pure Fe(OH)$_x$, Rh/Al_2O_3 and Au/Fe_2O_3 as references. As shown in Fig. 3 and Table 2, the only one reduction peak of Rh/Al_2O_3 is centered at 108 °C. The closely resembled H_2 consumption amount of 404 μmol g_{cat}^{-1} to the theoretical value for the reduction of Rh^{3+} to Rh^0 (437 μmol g_{cat}^{-1}) suggests that only the Rh species on Rh/Al_2O_3 is reduced. As for pure Fe(OH)$_x$, there are two major peaks: the high-temperature peak (T_H) at 713 °C attributed to the reduction of bulk Fe_2O_3 and the low-temperature one (T_L) at 315 °C

Table 1
Physicochemical properties of the synthesized catalysts.

sample	Rh loadings (wt.%)	S_{BET} (m^2 g^{-1})	B.E. of Rh3d$_{5/2}$ (eV)	B.E. of Fe2p$_{3/2}$ (eV)	CO uptake (μmol $g_{cat.}^{-1}$)	O_2 uptake (μmol $g_{cat.}^{-1}$)
Rh/Fe(OH)$_x$	3.1	298	307.0, 308.5	709.8, 712.1	27	2065
Rh/Al_2O_3	3.0	314	307.1	–	237	143

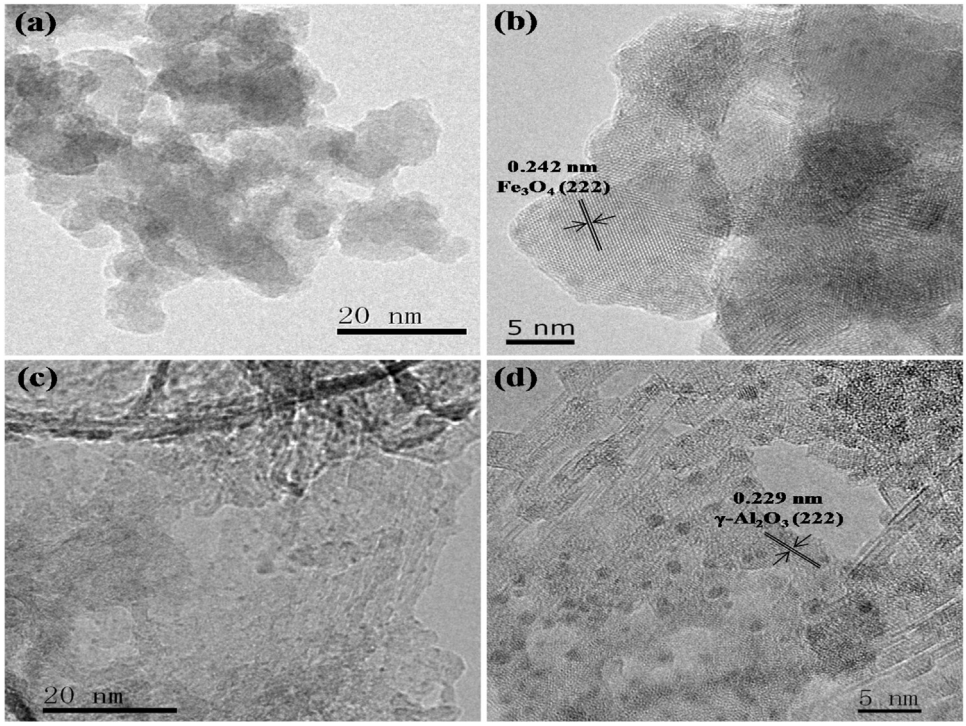

Fig. 2. HR-TEM images of (a, b) $Rh/Fe(OH)_x$ and (c, d) Rh/Al_2O_3 catalysts. All the samples were prereduced at 200 °C for 30 min with 10% H_2/He.

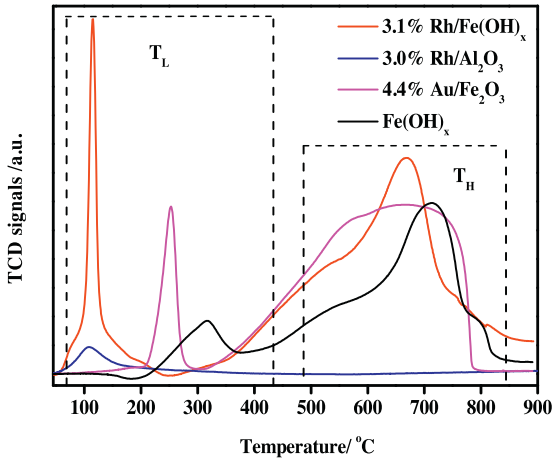

Fig. 3. H_2-TPR profiles of the $Rh/Fe(OH)_x$, Rh/Al_2O_3, Au/Fe_2O_3 catalysts and $Fe(OH)_x$ support.

Table 2
Reducibility of the catalyst as measured by H_2-TPR.

	H_2 consumed ($\mu mol\, g_{cat}^{-1}$)	
	Peak I (T_L/°C)	Peak II (T_H/°C)
$Fe(OH)_x$	996 (315)	8286 (713)
$Rh/Fe(OH)_x$	2522 (115)	11154 (668)
Rh/Al_2O_3	404 (108)	–
Au/Fe_2O_3	1434 (253)	12170 (666)

to the surface Fe_2O_3. With the loading of Rh, the T_L of $Rh/Fe(OH)_x$ is greatly decreased to 115 °C with H_2 consumption amount of 2522 $\mu mol\, g_{cat}^{-1}$. It is about 5.5 times of the theoretical value for the reduction of Rh^{3+} to Rh^0 (452 $\mu mol\, g_{cat}^{-1}$), indicating that not only Rh but also surface Fe^{3+} species are reduced at this temperature, thus further corroborating the presence of Fe_3O_4 phases in the reduced samples. Comparatively, the Au/Fe_2O_3 shows a higher T_L for the reduction of surface Fe^{3+} species and a lower H_2 consumption amount of 1434 $\mu mol\, g_{cat}^{-1}$. These results suggest that the reducibility of $Fe(OH)_x$ support was greatly improved, probably due to the strong interaction with the highly dispersed Rh clusters as verified in the Pt, Pd/FeO_x systems [40].

The chemical states of Rh species of the reduced samples were obtained by XPS characterization and the results are shown in Fig. 4 and Table 1. For Rh/Al_2O_3 catalyst, Rh species are fully reduced to metallic (Rh^0) state with binding energy of 307.1 eV. Comparatively, apart from the Rh^0 species with binding energy of 307.0 eV, $Rh/Fe(OH)_x$ catalyst shows additional binding energy of 308.5 eV, lying between the reported value for Rh^0 (~307.0 eV) and Rh^{3+} (~309.4 eV) [24,25]. It means that some Rh species are present as positively charged state ($Rh^{\delta+}$, $0 < \delta < 3$). Moreover, the binding energies of Fe species are 709.8 and 712.0 eV, which represent the Fe^{2+} and Fe^{3+}, respectively [36] and manifest the partial reduction of $Fe(OH)_x$ support. These results indicate the existence of the electron transfer between the subnano Rh clusters and $Fe(OH)_x$ support after the reduction treatment.

The structure characterizations illustrate that a novel catalyst formulation with subnano Rh clusters uniformly dispersed on the $Fe(OH)_x$ support was successfully fabricated. The metal-support interaction and electron transfer between them result in the positively charged $Rh^{\delta+}$ species and enhanced reducibility of the $Fe(OH)_x$ support.

3.2. Catalytic performance detects

Fig. 5a and b shows the profiles of CO conversion and selectivity for the PROX reaction as a function of reaction temperature. The Au/Fe_2O_3–WGC catalyst was tested first for its well-known high activity for oxidation of CO. The CO conversions over this catalyst are 100% at 20–40 °C and then gradually decrease with the reaction temperatures because of the competitive oxidation of H_2 as indicated by the gradual decrease of CO_2 selectivity. Comparatively, the $Rh/Fe(OH)_x$ catalyst exhibits better performance with total CO removal and almost stable selectivity around 50% at a wider tem-

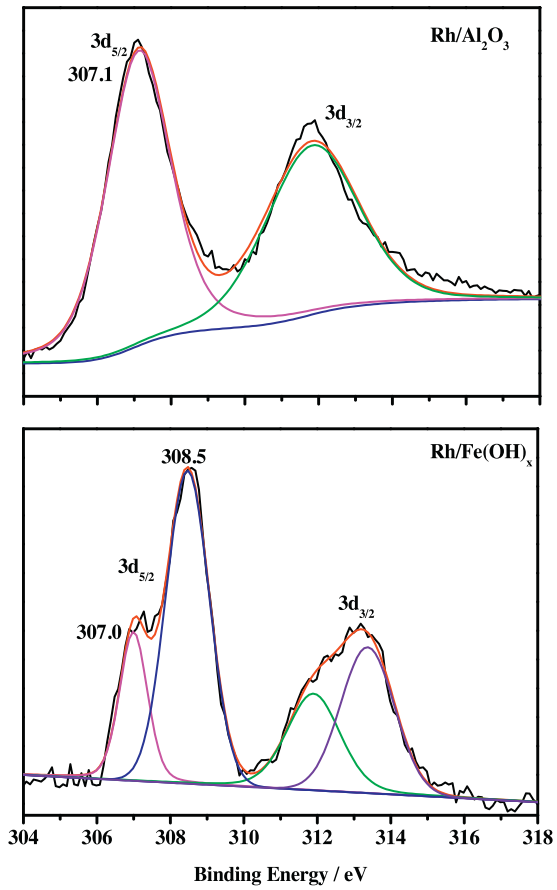

Fig. 4. XPS results of the reduced Rh/Al_2O_3 and $Rh/Fe(OH)_x$ catalysts.

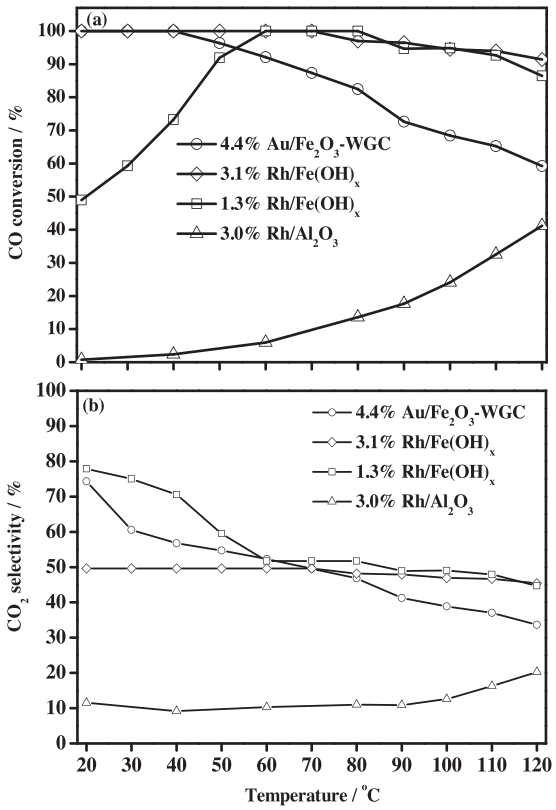

Fig. 5. (a) CO conversion and (b) CO_2 selectivity as a function of temperature for the PROX reaction, reaction conditions: 1 vol.% CO, 1 vol.% O_2, 40 vol.% H_2, WHSV: 18,000 mL h^{-1} g_{cat}^{-1}.

perature window of 20–70 °C despite of the lower metal loading of 3.1 wt.%. This sustainable high activity over a wider temperature range is practically beneficial considering the strong exothermic character of PROX (Eqs. (1) and (2)). Even for a lower Rh loading of 1.3 wt.%, it still exhibits high activity with 50% conversion at 20 °C and 100% conversion in the temperature range of 60–80 °C. For Rh/Al_2O_3, however, the CO conversions are negligible at room temperature and only 25% at temperatures higher than 100 °C. As shown in Table 3, when compared with the former reported Rh-based catalysts, such as Rh/MgO [41], Rh@Pt [42], Rh/3A [43], Rh/Nb_2O_5 [44], Rh/USY [45], Rh/Al_2O_3 [46], as well as the typical CuO/CeO_2 system [7], only $Rh/Fe(OH)_x$ catalyst is capable of total CO conversion at room temperatures.

To further show the intrinsic activity of $Rh/Fe(OH)_x$, the specific rates and TOFs were compared with the reported Rh-based catalysts in Table 4. The TOF for PROX (0.054 s^{-1}) on $Rh/Fe(OH)_x$ is around 3 times higher than that for CO oxidation (0.016 s^{-1}) at 27 °C, indicating the promotional effect of H_2 on low-temperature CO oxidation. While this value is in the same order of magnitude to those of Au/Fe_2O_3 (0.086 s^{-1}), illustrating their comparable activity. When comparing with the traditional Rh/Al_2O_3 as well as other Rh-based systems like polymer stabilized Rh NPs catalysts[24], Rh/CeO_2 [27] and Rh/USY [45], $Rh/Fe(OH)_x$ is orders of magnitude more active. These results unequivocally manifest the high activity of $Rh/Fe(OH)_x$ catalyst in the oxidation of CO.

Considering the inevitable presence of CO_2 and H_2O in the H_2 resource from reforming gases, we tested the CO_2 and H_2O resistance of $Rh/Fe(OH)_x$ and Au/Fe_2O_3 catalyst. As shown in Fig. 6a, with the presence of 20 vol.% CO_2, the CO conversion maintains as 100% for 320 min, then slowly decreases to 89% after 700 min over $Rh/Fe(OH)_x$, while it decays quickly from the original 85% to 62% after 260 min over Au/Fe_2O_3 catalyst. These results indicate that the $Rh/Fe(OH)_x$ shows a better CO_2 tolerance ability. The addition of 3 vol.% H_2O improves the stability. Particularly, $Rh/Fe(OH)_x$ catalyst still shows a much longer term activity with total CO removal of 520 min while the conversions of Au/Fe_2O_3 quickly decrease from the original 100% to only 70% in 260 min. The addition of more

Table 3
Comparative activity results of PROX reaction over reported catalysts in terms of conversion.

Catalyst system	Reaction gas composition	Con.	Sel.	T/°C	Note
4.4% Au/Fe–WGC	40% H_2, 1% CO, 1% O_2	100%	52%	20	This work
3.1% $Rh/Fe(OH)_x$	40% H_2, 1% CO, 1% O_2	100%	53%	20	This work
3.0% Rh/Al_2O_3	40% H_2, 1% CO, 1% O_2	42%	20%	120	This work
0.5% Rh/MgO	75% H_2, 1% CO, 1% O_2	100%	40%	175	[41]
Rh@Pt/γ–Al_2O_3	50% H_2, 0.2% CO, 0.5% O_2	100%	55%	70	[42]
1% Rh/3A	37% H_2, 1% CO, 2% O_2	100%	25%	80	[43]
0.5% Rh/Nb_2O_5	3% H_2, 0.2% CO, 1% O_2	100%	20%	100	[44]
K-2% Rh/USY	75% H_2, 1% CO, 1% O_2	100%	50%	130	[45]
K-2%Rh/Al_2O_3	40% H_2, 1% CO, 1% O_2	100%	50%	222	[46]
0.15% CuO/CeO_2	50% H_2, 1% CO, 1.25% O_2	95%	100%	140	[7]

Table 4
Comparative activity results of CO oxidation and PROX reaction over Rh-based catalysts in terms of TOFs and specific reaction rates.

Catalysts system	Reactiontype	T/°C	Specific rates × 10^2 [$mol_{co}\ h^{-1}\ g_{metal}^{-1}$]	TOF × 10^2 [s^{-1}]	Note
Au/Fe_2O_3–WGC	PROX	27	39.3	8.6	This work[a]
$Rh/Fe(OH)_x$	PROX	27	19.3	5.4	This work[b]
Rh/Al_2O_3	PROX	80	5.8	0.2	This work[b]
K-Rh/USY	PROX	110	–	4.2	[45][c]
Au/Fe_2O_3–WGC	CO oxi.	27	22.0	4.7	This work[a]
$Rh/Fe(OH)_x$	CO oxi.	27	5.9	1.6	This work[b]
Rh/Al_2O_3	CO oxi.	80	7.3	0.3	This work[b]
2 nm Rh NPs	CO oxi.	27	0.82	0.052[f]	[24][d]
Rh/CeO_2	CO oxi.	27	–	0.024[g]	[27][e]
K-Rh/USY	CO oxi.	110	–	4.0	[45][c]

TOFs were calculated based on the metal dispersion. The metal dispersion was measured with
[a] the relationship between the degree of dispersion and particle size, i.e., $D = 1/d_{Au}$.
[b] microcalorimetric experiments of CO adsorption by assuming CO/Rh = 1/1.
[c] volumetric method of H_2 chemisorption in a vacuum system by assuming H/Rh = 1/1.
[d] the relationship between the degree of dispersion and particle size, i.e., $D = 1/d_{Rh}$.
[e] H_2 chemisorption measurements carried out at −80 °C by assuming H/Rh = 1/1.
[f] TOF at 27 °C was derived from the TOF at 200 °C and Ea.
[g] TOF at 27 °C was derived from the TOF at 60 °C and Ea.

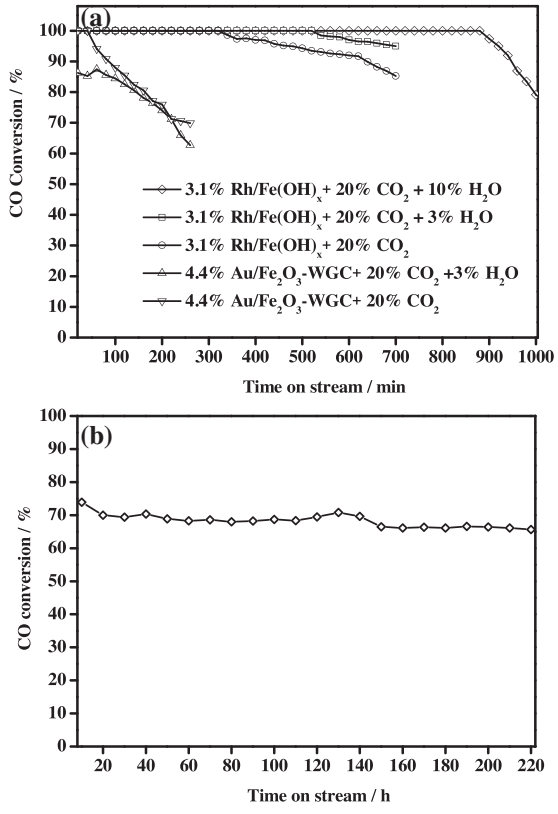

Fig. 6. (a) CO_2 and H_2O resistance of $Rh/Fe(OH)_x$ and Au/Fe_2O_3 catalyst at 50 °C, reaction conditions: 1 vol.% CO, 1 vol.% O_2, 40 vol.% H_2, 20 vol.% CO_2 with or without 3/10 vol.% H_2O, WHSV: 18,000 mL h^{-1} $g_{cat.}^{-1}$; (b) Stability of 3.1 wt.% $Rh/Fe(OH)_x$ at 80 °C, reaction conditions: 1 vol.% CO, 1 vol.% O_2, 40 vol.% H_2, WHSV: 21,000 mL h^{-1} $g_{cat.}^{-1}$.

concentration of H2O (10 vol.%) further prolongs the period for total CO conversion prolongs to 880 min. The significant positive effect of water has been observed in other catalyst systems and are mainly attributed to the enhancement of the water–gas-shift reaction, formation of hydroxyl groups and the promotion of the decomposition of carbonates [47–49]. In our previous work on the effect of hydroxyl species on CO oxidation over $Ir/Fe(OH)_x$ catalyst [34], we found that H_2O can react with the adsorbed O to produce hydroxyl species, which can readily react with CO and also prohibit the accumulation of carbonates. Accordingly, we think that water probably plays a similar role for $Rh/Fe(OH)_x$ and improves its H_2O resistance and stability. Furthermore, we also investigated the stability of this $Rh/Fe(OH)_x$ catalyst at the working temperature of PEMFC (80 °C) at higher space velocity to avoid 100% CO conversion. As shown in Fig. 6b, the CO conversions keep constant of around 70% for 220 h run. These results show promising application of our $Rh/Fe(OH)_x$ catalyst for PROX reaction.

The $Rh/Fe(OH)_x$ catalyst shows a comparable activity level with standard gold catalyst but a wider temperature range for CO total removal and better tolerance to CO_2 and H_2O. The dramatically enhanced activity compared with other Rh catalysts indicates the crucial role of $Fe(OH)_x$ support in the low temperature oxidation of CO.

3.3. The factors for the high performance of $Rh/Fe(OH)_x$

It is well accepted that the weakening of CO adsorption and/or the promoting of O_2 activation is critical to enhance the low-temperature activity for the oxidation of CO [35–38]. Herein, CO/O_2 adsorption microcalorimetry, in situ DRIFTS measurements and kinetic studies were conducted to explore the factors for such high performance of CO oxidation over $Rh/Fe(OH)_x$ catalyst.

3.3.1. Adsorption microcalorimetry

Adsorption microcalorimetry is a powerful tool to evaluate the adsorption strength and amount of a certain probe gas, which is quantified in terms of initial adsorption heat and saturation uptake, respectively [50]. As shown in Fig. 7a, the initial adsorption heat of CO is quite high on Rh/Al_2O_3 (121 kJ mol^{-1}), whereas it decreases to 97 kJ mol^{-1} for $Rh/Fe(OH)_x$. On the other hand, the CO uptake on $Rh/Fe(OH)_x$ (27 μmol g_{cat}^{-1}) is around one order of magnitude lower than that on Rh/Al_2O_3 (237 μmol g_{cat}^{-1}). These results suggest that the CO adsorption is largely weakened, probably resulted from the covering of Rh by the partially reduced $Fe(OH)_x$ or the reduced electron back-donation to the adsorbed CO on the positive $Rh^{\delta+}$ clusters.

The O_2 adsorption abilities are compared in Fig. 7b. The initial adsorption heat on Rh/Al_2O_3 is 361 kJ mol^{-1}, similar to the oxidation heat of metallic Rh surface (343 kJ mol^{-1}) [51]. The saturation uptake is only 143 μmol g_{cat}^{-1}, lower than the theoretical amount for the oxidation of Rh to Rh_2O_3 (228 μmol g_{cat}^{-1}), indicating that Rh^0 serves as the main sites for O_2 adsorption. Comparatively, this amount is sharply increased to 2065 μmol g_{cat}^{-1} on $Rh/Fe(OH)_x$, which is not solely resulted from the O_2 adsorption on Rh sites (topmost 226 μmol g_{cat}^{-1} based on Rh loading) but also from that on the support. The initial adsorption heat of 465 kJ mol^{-1}, closely resemble to the oxidation heat of the Fe^{2+} species to Fe^{3+} species (460 kJ mol^{-1}) [50], further confirms the importance of support in

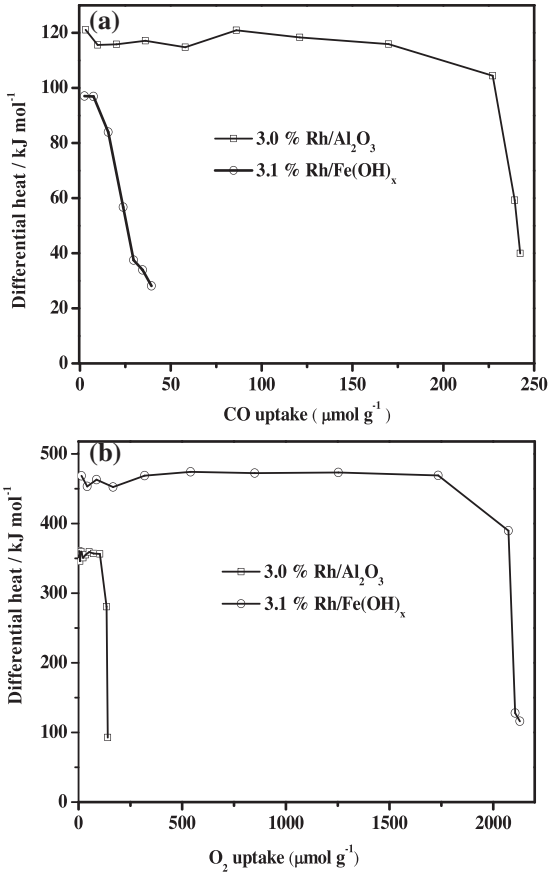

Fig. 7. Microcalorimetry results of (a) CO and (b) O_2 adsorption on Rh/Fe(OH)$_x$ and Rh/Al_2O_3 catalysts.

O_2 adsorption and activation. Thus, the adsorption microcalorimetric results quantitatively prove the weakening of CO adsorption as well as the activation and O_2 over the Rh/Fe(OH) *x*catalyst in CO oxidation.

3.3.2. *In situ DRIFTS measurements*

In situ DRIFTS measurements were carried out under CO adsorption and CO oxidation conditions for further insights into the adsorption and reaction properties of Rh/Fe(OH)$_x$ catalyst.

As shown in Fig. 8, the adsorption of CO on Rh/Al_2O_3 produces two bands at 2055 and 1860 cm^{-1}, which are assigned to the linearly and bridged bonded CO on Rh^0 sites, respectively, together with the doublet peaks of gem-carbonyl species [$Rh^I(CO)_2$] at 2088 and 2020 cm^{-1}. In comparison, there is only gem-carbonyl species at 2091 and 2022 cm^{-1} over the Rh/Fe(OH)$_x$ catalyst. Moreover, the band intensity is around one order of magnitude weaker than that on Rh/Al_2O_3, which is in good line with the adsorption microcalorimetric results. The DRIFTS result also verifies the high dispersion of subnano $Rh^{\delta+}$ clusters over Rh/Fe(OH)$_x$ in view of the necessity of relatively high dispersions and sufficiently small particle sizes for the IR detection of only $Rh^I(CO)_2$ species [52,53].

The reaction behavior of these adsorbed CO species with O_2 was further studied. As shown in Fig. 9a, with the addition of O_2 onto the CO-saturated Rh/Al_2O_3 catalyst, the peaks of linearly and bridged adsorbed CO is blue shifted to higher frequencies (from 2055 to 2060 cm^{-1} and 1862 to 1888 cm^{-1}, respectively) with production of small amounts of CO_2. This indicates a competitive adsorption of O_2 with CO on the Rh sites, which causes the decreased back-donation of electrons from Rh to CO and the blue-shift. Comparatively, as shown in Fig. 9b, no relevant shift is observed over Rh/Fe(OH)$_x$ with large amount of CO_2 produced. It suggests that unlike Rh/Al_2O_3, the

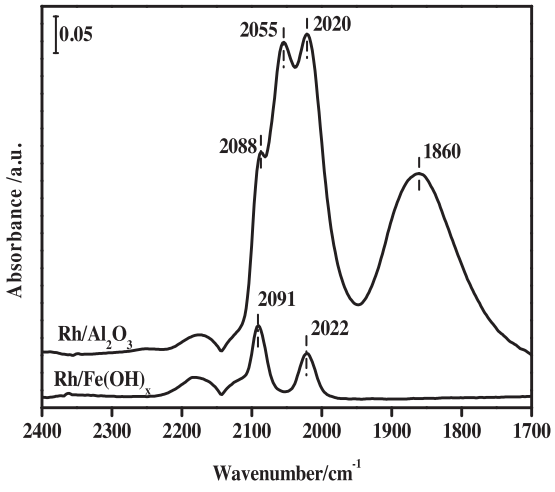

Fig. 8. In situ DRIFTS spectra of CO adsorption over Rh/Fe(OH)$_x$ and Rh/Al_2O_3 catalysts.

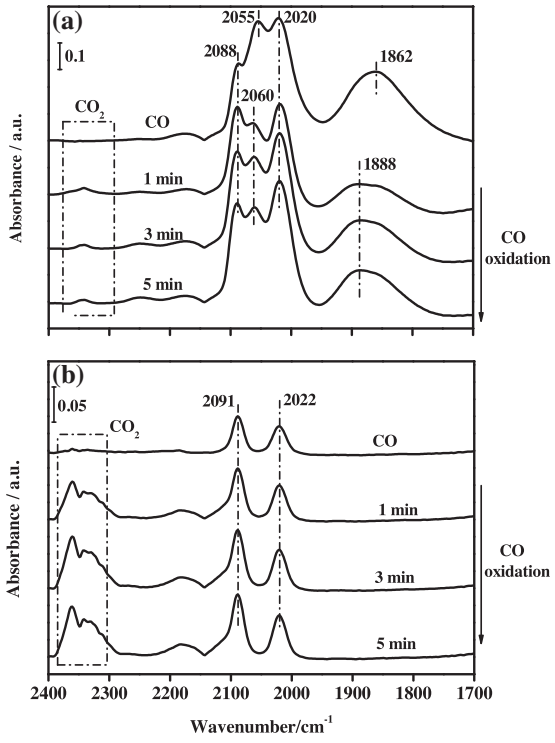

Fig. 9. In situ DRIFTS spectra of CO oxidation with time on stream over (a) Rh/Al_2O_3 and (b) Rh/Fe(OH)$_x$ catalysts saturated with CO.

Rh/Fe(OH)$_x$ catalyst can provide dual sites for CO oxidation, that is, CO adsorbed on Rh sites reacts with the uncompetitively adsorbed O_2 on Fe(OH)$_x$ sites.

3.3.3. *Kinetic detects*

The kinetic behavior of catalytic reactions has been proved as primary information for their underlying mechanisms and reaction pathways [54,55]. Reaction orders and apparent activation energies (Ea) for the oxidation of CO were calculated for kinetic-based elucidation of the superior activity over Rh/Fe(OH)$_x$.

As shown in Fig. 10a and b, the reaction order of CO and O_2 over Rh/Al_2O_3 is −0.29 and 0.82, respectively. The negative α_{CO} is a direct indication of CO inhibition effect on the O_2 adsorption on Rh surface, as verified in the DRIFTS experiments in Fig. 9a. The derived rate equation of $r = k_0[CO]^{-0.29}[O_2]^{0.82}$ indicates the oxida-

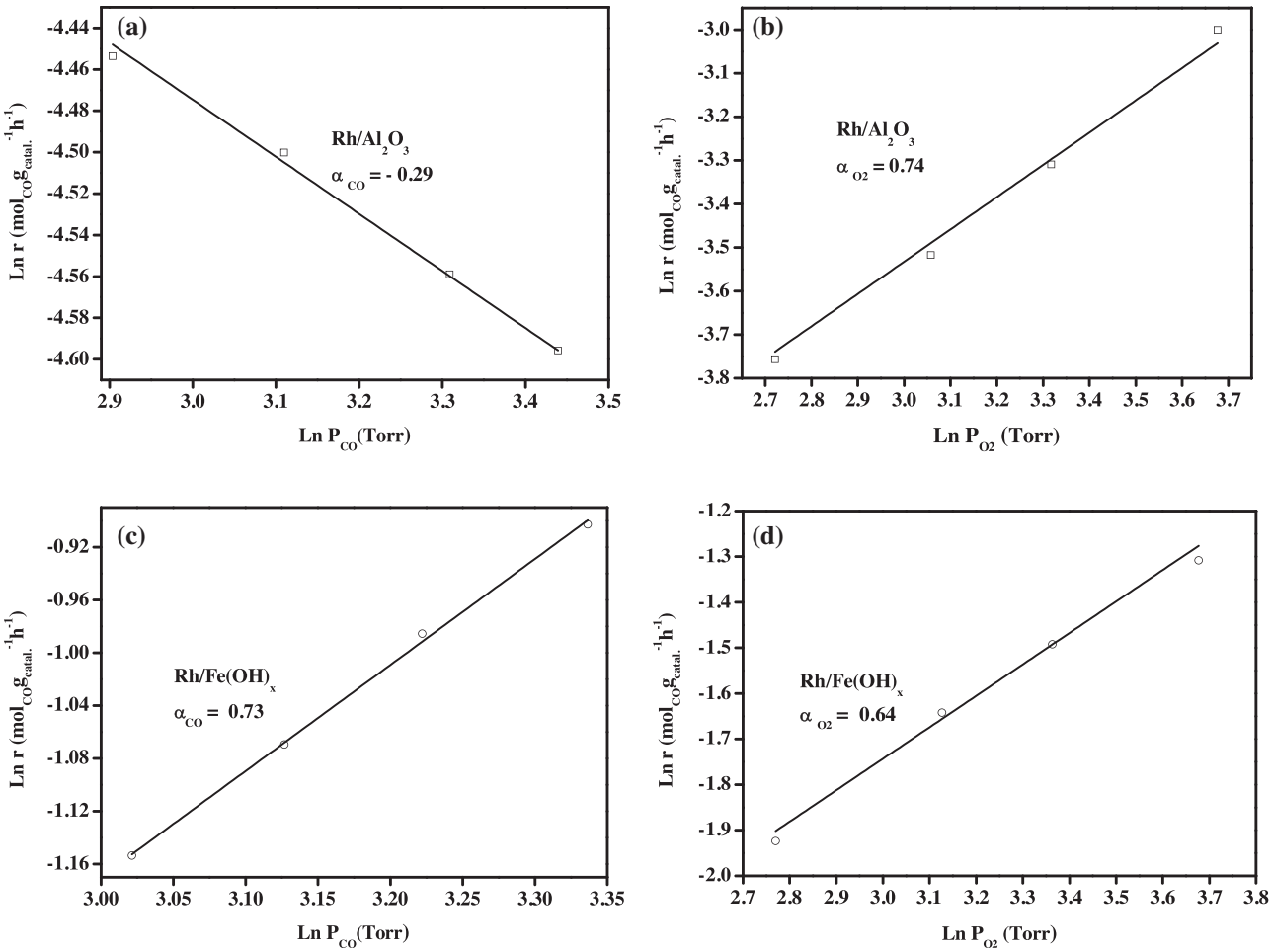

Fig. 10. Reaction orders of CO and O_2 for the CO oxidation over (a, b) Rh/Al_2O_3 and (c, d) $Rh/Fe(OH)_x$ catalysts at 80 °C.

tion of CO proceeds with a competitive L–H mechanism, which is characterized with a negative α_{CO} with the adsorption and/or activation O_2 as rate determining step [54–56]. In this way, its poor activity at low temperatures could be explained with the unavailability of active oxygen species; no virtually reaction would occur until the temperature is high enough to desorb significant amount of CO for O_2 activation.

With the reaction orders calculated from the corresponding plots in Fig. 10c and d, the rate equation for the oxidation of CO over $Rh/Fe(OH)_x$ catalyst is established as $r = k[CO]^{0.73}[O_2]^{0.64}$. The rollover from negative to positive α_{CO} suggest the transition to a non-competitive L–H mechanism, which arises from the vanishing of the CO inhibition effect and more importantly, the activation of oxygen species on $Fe(OH)_x$ support. Meanwhile, the decrease of α_{O2} indicates that the more efficient O_2 activation leads to a weaker dependence of the reaction rates on the oxygen pressures, correlating well with the deduced rate determining step of the elementary reaction between $CO_{(ad)}$ and $O_{(ad)}$ for the non-competitive L-H mechanism model [54,56]. The change of rate determining step can result in the smaller apparent activation energy of 24 kJ mol^{-1} compared with 43 kJ mol^{-1} over Rh/Al_2O_3 catalyst (Fig. 11).

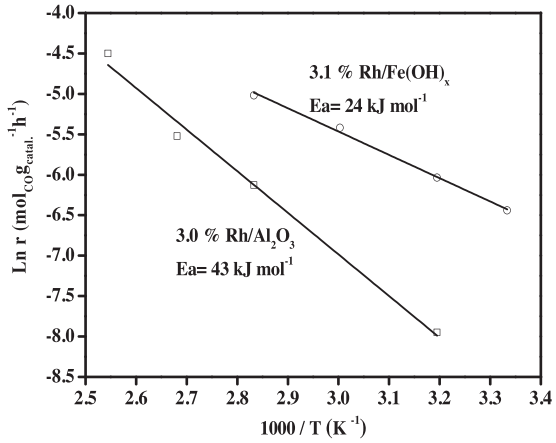

Fig. 11. Arrhenius plot for CO oxidation over $Rh/Fe(OH)_x$ and Rh/Al_2O_3 catalysts.

4. Discussion

It has been found that $Fe(OH)_x$ is a special support with a longer Fe—O bond and rich of surface OH groups than traditional Fe_2O_3 [57]. The longer Fe—O bond favors its higher reducibility, which usually explained the high activity of $Fe(OH)_x$-supported noble metals catalysts for low temperature CO oxidation [40,58,59]. The OH species help to stabilize supported metal species in a form of subnano or even single atoms [37,38,60,61], which can change the adsorption properties for CO. The positive single atom Pt species on $Pt/Fe(OH)_x$ exhibited weaker CO adsorption compared with nano-sized Pt species [37,38]. While for $Pd/Fe(OH)_x$ system, it was the variation of CO adsorption mode that changed its adsorption strength; the dominantly linear adsorptions of CO rather than the bridged ones led to weaker strength [60]. In this work, the Rh species over the $Rh/Fe(OH)_x$ catalyst are highly dispersed as posi-

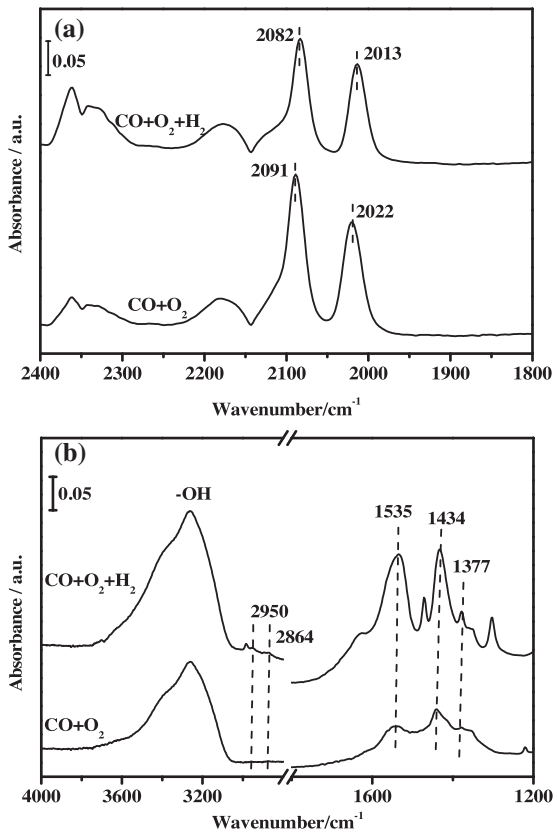

Fig. 12. In situ DRIFTS spectra of CO oxidation and PROX under steady state over $Rh/Fe(OH)_x$ catalyst.

tive charged subnano clusters according to XPS in Fig. 4 and HRTEM images in Fig. 2. The DRIFTS results in Fig. 8 reveal the presence of only weakly adsorbed gem-carbonyl species as $Rh^I(CO)_2$ with smaller band intensity but without linear or bridged ones compared with that on Rh/Al_2O_3, which confirm the decreased strength of CO adsorption from nano to subnano Rh species. Moreover, the CO adsorption microcalorimetric in Fig. 7a quantitatively support this indication. The weakened CO adsorption dictates the positive reaction order of CO for the oxidation of CO, thus solving the dilemma of prohibition effect of the strong CO adsorption on PGM-based catalyst like Rh/Al_2O_3 which shows a negative CO reaction order.

On the other hand, the O_2 adsorption and activation is also greatly facilitated on the $Rh/Fe(OH)_x$ catalyst. The H_2-TPR results suggest that the Rh species promote the reduction of $Fe(OH)_x$, which can create more vacancy sites. The O_2 adsorption microcalorimetric results in Fig. 7b indicate that its large uptake amount is not attributed solely to the adsorption on Rh sites but more importantly to that on the support, that is, the partial reduced $Fe(OH)_x$ is the main sites for O_2 adsorption. The in situ DRIFTS results in Fig. 9b further approve that it is the oxygen species on the support that reacts with CO on Rh sites in the oxidation of CO, while these active oxygen species might come from the contribution of surface molecular ones or the lattice oxygen [62]. Consequently, the much more oxygen species on $Rh/Fe(OH)_x$ than those on Rh/Al_2O_3 resulted in a rather weaker dependence of the reaction rates on the oxygen pressures.

The weakened adsorbed CO on Rh sites and the facilitated adsorbed O_2 on $Fe(OH)_x$ permit a non-competitive L–H mechanism for the low temperature oxidation of CO over $Rh/Fe(OH)_x$ catalyst. Along with this reaction mechanism, another important factor is the promoting role of H_2 as shown in the intrinsic activity results in Table 4. One of the H_2 promoting effects is that it can be oxidized to hydroxyl species, which then react with CO [34,63]. An in situ DRIFTS study after addition of H_2 to the CO oxidation on $Rh/Fe(OH)_x$ was performed herein. As shown in Fig. 12a, adding H_2 shifts the band of Rh—CO from the original 2091 and 2020 cm^{-1} to 2082 and 2013 cm^{-1}, respectively. The red-shift can be attributed to enhanced back donation from Rh to CO by forming an Rh—H bond, that is, the competitive adsorption of H_2 and CO on Rh sites. Furthermore, as shown in Fig. 12b, there are more OH species coupled with production of more CO_2. These results indicate that the adsorbed H species can react with the adsorbed O_2 on $Fe(OH)_x$ to form OH species. Moreover, the bands (2950, 2864, 1535, 1434 and 1377) attributed to formate species are either newly formed or greatly increased after the addition of H_2, which has been proposed as intermediate due to the reaction between the OH species and CO [64–67]. This result suggest that the remarkable effect of OH species on low-temperature CO oxidation also work on this $Rh/Fe(OH)_x$, just like the previous study on $Ir/Fe(OH)_x$ catalyst [34]. On the other hand, when we fed 0.6% H_2O to the reacting gas of CO oxidation, the CO conversion increased from 37% to 100% at 20 °C, which might be promoted by the OH species from $O + H_2O \rightarrow 2OH$. For the formation of OH species by the addition of H_2 or H_2O, the presence of the facilitated adsorbed O_2 on $Fe(OH)_x$ was prerequisite. As a result, a novel Rh-based catalyst with high performance of total CO removal at a wide temperature range of 20–70 °C was obtained for the first time and the origin of its superior activity was well rationalized with detailed characterizations. It not only enriched the efficient PROX catalyst family but also presented quotable reference for the fabrication of novel catalyst for the efficient oxidation of CO.

5. Conclusion

In summary, we have fabricated a novel highly efficient PGM-based catalyst via a co-precipitation method for PROX, that is, $Rh/Fe(OH)_x$. This catalyst exhibits comparable turnover frequency (TOF) with the standard gold catalyst of Au/Fe_2O_3 but a wider temperature range of 20–70 °C for CO total conversion and better tolerance to CO_2 and H_2O. The Rh species are uniformly dispersed as subnano clusters with sizes around 1 nm, which can promote the partial reduction of $Fe(OH)_x$ support. The CO adsorption is much weakened on these subnano Rh species while the O_2 adsorption is greatly promoted on the $Fe(OH)_x$ support. This permits the oxidation of CO over $Rh/Fe(OH)_x$ to follow a non-competitive L–H mechanism with the surface reaction between $CO_{(ad)}$ and $O_{(ad)}$ as the rate determining step and a small activation energy. The presence of H_2 can further promote the oxidation of CO through the formation of OH species. In this way, the superior reactivity of this Rh-based catalyst in PROX reaction is well rationalized with the mutual authenticated results from adsorption characterizations and kinetic studies.

Acknowledgment

Financial supports for this research work from the National Natural Science Foundation of China (21076211, 21173218, 21203181, 21576251) are gratefully acknowledged.

Appendix A. Supplementary data

Supplementary data associated with this article can be found, in the online version, at http://dx.doi.org/10.1016/j.apcatb.2015.11.040.

References

[1] O. Korotkikh, R. Farrauto, Catal. Today 62 (2000) 249–254.
[2] E.D. Park, D. Lee, H.C. Lee, Catal. Today 139 (2009) 280–290.

[3] K. Liu, A. Wang, T. Zhang, ACS Catal. 2 (2012) 1165–1178.
[4] G. Avgouropoulos, T. Ioannides, H.K. Matralis, J. Batista, S. Hocevar, Catal. Lett. 73 (2001) 33–40.
[5] P. Ratnasamy, D. Srinivas, C.V.V. Satyanarayana, P. Manikandan, R.S.S. Kumaran, M. Sachin, V.N. Shetti, J. Catal. 221 (2004) 455–465.
[6] G. Avgouropoulos, T. Ioannides, H. Matralis, Appl. Catal. B-Environ. 56 (2005) 87–93.
[7] G. Avgouropoulos, T. Ioannides, Appl. Catal. B-Environ. 67 (2006) 1–11.
[8] C. Tang, J. Sun, X. Yao, Y. Cao, L. Liu, C. Ge, F. Gao, L. Dong, Appl. Catal. B-Environ. 146 (2014) 201–212.
[9] G. Avgouropoulos, T. Ioannides, Appl. Catal. A-Gen. 244 (2003) 155–167.
[10] A. Arango-Diaz, J.A. Cecilia, E. Moretti, A. Talon, P. Nunez, J. Marrero-Jerez, J. Jimenez-Jimenez, A. Jimenez-Lopez, E. Rodriguez-Castellon, Int. J. Hydrogen Energy 39 (2014) 4102–4108.
[11] D. Gamarra, A. Lopez Camara, M. Monte, S.B. Rasmussen, L.E. Chinchilla, A.B. Hungria, G. Munuera, N. Gyorffy, Z. Schay, V. Cortes Corberan, J.C. Conesa, A. Martinez-Arias, Appl. Catal. B-Environ. 130 (2013) 224–238.
[12] E. Moretti, L. Storaro, A. Talon, P. Riello, A.I. Molina, E. Rodriguez-Castellon, Appl. Catal. B-Environ. 168 (2015) 385–395.
[13] M. Haruta, S. Tsubota, T. Kobayashi, H. Kageyama, M.J. Genet, B. Delmon, J. Catal. 144 (1993) 18.
[14] R.M.T. Sanchez, A. Ueda, K. Tanaka, M. Haruta, J. Catal. 168 (1997) 125–127.
[15] P. Landon, J. Ferguson, B.E. Solsona, T. Garcia, A.F. Carley, A.A. Herzing, C.J. Kiely, S.E. Golunski, G.J. Hutchings, Chem. Commun. (2005) 3385–3387.
[16] Q.Q. Lin, B.T. Qiao, Y.Q. Huang, L. Li, J. Lin, X.Y. Liu, A.Q. Wang, W.C. Li, T. Zhang, Chem. Commun. 50 (2014) 2721–2724.
[17] M. Shelef, G.W. Graham, Catal. Rev. Sci. Eng. 36 (1994) 433–457.
[18] M. Shelef, R.W. McCabe, Catal. Today 62 (2000) 35–50.
[19] M.V. Twigg, Appl. Catal. B-Environ. 70 (2007) 2–15.
[20] J.A. Kurzman, L.M. Misch, R. Seshadri, Dalton Trans. 42 (2013) 14653–14667.
[21] H.J. Freund, G. Meijer, M. Scheffler, R. Schlogl, M. Wolf, Angew. Chem. Int. Ed. 50 (2011) 10064–10094.
[22] C.H.F. Peden, D.W. Goodman, D.S. Blair, P.J. Berlowitz, G.B. Fisher, S.H. Oh, J. Phys. Chem. 92 (1988) 1563–1567.
[23] S. Blomberg, R. Westerstrom, N.M. Martin, E. Lundgren, J.N. Andersen, M.E. Messing, J. Gustafson, Surf. Sci. 628 (2014) 153–158.
[24] M.E. Grass, Y. Zhang, D.R. Butcher, J.Y. Park, Y. Li, H. Bluhm, K.M. Bratlie, T. Zhang, G.A. Somorjai, Angew. Chem. Int. Ed. 47 (2008) 8893–8896.
[25] S.M. Kim, K. Qadir, B. Seo, H.Y. Jeong, S.H. Joo, O. Terasaki, J.Y. Park, Catal. Lett. 143 (2013) 1153–1161.
[26] S.H. Oh, C.C. Eickel, J. Catal. 128 (1991) 526–536.
[27] D.A. Ligthart, R.A. van Santen, E.J. Hensen, Angew. Chem. Int. Ed. 50 (2011) 5306–5310.
[28] V. Rico Pérez, M. Ángeles Velasco Beltrán, Q. He, Q. Wang, C. Salinas Martínez de Lecea, A. Bueno López, Catal. Commun. 33 (2013) 47–50.
[29] R.H. Nibbelke, A.J.L. Nievergeld, J. Hoebink, G.B. Marin, Appl. Catal. B-Environ. 19 (1998) 245–259.
[30] X. Liu, O. Korotkikh, R. Farrauto, Appl. Catal. A-Gen. 226 (2002) 293–303.
[31] A. Siani, O.S. Alexeev, G. Lafaye, M.D. Amiridis, J. Catal. 266 (2009) 26–38.
[32] M. Kotobuki, A. Watanabe, H. Uchida, H. Yamashita, M. Watanabe, J. Catal. 236 (2005) 262–269.
[33] W. Zhang, A. Wang, L. Li, X. Wang, T. Zhang, Catal. Today 131 (2008) 457–463.
[34] J. Lin, B. Qiao, L. Li, H. Guan, C. Ruan, A. Wang, W. Zhang, X. Wang, T. Zhang, J. Catal. 319 (2014) 142–149.
[35] J. Lin, B. Qiao, J. Liu, Y. Huang, A. Wang, L. Li, W. Zhang, L.F. Allard, X. Wang, T. Zhang, Angew. Chem. Int. Ed. 51 (2012) 2920–2924.
[36] Q. Fu, W. Li, Y. Yao, H. Liu, H. Su, D. Ma, X. Gu, L. Chen, Z. Wang, H. Zhang, B. Wang, X. Bao, Science 328 (2010) 1141–1144.
[37] B. Qiao, A. Wang, L. Li, Q. Lin, H. Wei, J. Liu, T. Zhang, ACS Catal. 4 (2014) 2113–2117.
[38] B. Qiao, A. Wang, X. Yang, L.F. Allard, Z. Jiang, Y. Cui, J. Liu, J. Li, T. Zhang, Nat. Chem. 3 (2011) 8.
[39] K. Zhao, H. Tang, B. Qiao, L. Li, J. Wang, ACS Catal. 5 (2015) 3528–3539.
[40] L. Liu, F. Zhou, L. Wang, X. Qi, F. Shi, Y. Deng, J. Catal. 274 (2010) 1–10.
[41] Y.F. Han, M.J. Kahlich, M. Kinne, R.J. Behm, Appl. Catal. B-Environ. 50 (2004) 209–218.
[42] S. Alayoglu, B. Eichhorn, J. Am. Chem. Soc. 130 (2008) 17479–17486.
[43] C. Galletti, S. Specchia, G. Saracco, V. Specchia, Ind. Eng. Chem. Res. 47 (2008) 5304–5312.
[44] S. Ito, T. Fujimori, K. Nagashima, K. Yuzaki, K. Kunimori, Catal. Today 57 (2000) 247–254.
[45] H. Tanaka, S. Ito, S. Kameoka, K. Tomishige, K. Kunimori, Appl. Catal. A-Gen. 250 (2003) 255–263.
[46] G.W. Chen, Q. Yuan, H.Q. Li, S.L. Li, Chem. Eng. J. 101 (2004) 101–106.
[47] X. Liao, W. Chu, X. Dai, V. Pitchon, Appl. Catal. B-Environ. 142 (2013) 25–37.
[48] T.R. Reina, E. Papadopoulou, S. Palma, S. Ivanova, M.A. Centeno, T. Ioannides, J.A. Odriozola, Appl. Catal. B-Environ. 150 (2014) 554–563.
[49] T.R. Reina, S. Ivanova, M.A. Centeno, J.A. Odriozola, Int. J. Hydrogen Energy 40 (2015) 1782–1788.
[50] A.K. Tripathi, V.S. Kamble, N.M. Gupta, J. Catal. 187 (1999) 332–342.
[51] D.R. Lide, Standard thermodynamic properties of chemical substances, in: CRC Handbook of Chemistry and Physics, 82nd ed., CRC Press, Inc., Boca Raton, Florida, 2000, pp. pp. 233.
[52] J.T. Yates, T.M. Duncan, S.D. Worley, R.W. Vaughan, J. Chem. Phys. 70 (1979) 6.
[53] J.C. Matsubu, V.N. Yang, P. Christopher, J. Am. Chem. Soc. 137 (2015) 3076–3084.
[54] G. Djega-Mariadassou, M. Boundart, J. Catal. 216 (2003) 89–97.
[55] A.D. Allian, K. Takanabe, K.L. Fujdala, X. Hao, T.J. Truex, J. Cai, C. Buda, M. Neurock, E. Iglesia, J. Am. Chem. Soc. 133 (2011) 4498–4517.
[56] N. Li, Q. Chen, L. Luo, W. Huang, M. Luo, G. Hu, J. Lu, Appl. Catal. B-Environ. 142–143 (2013) 523–532.
[57] P. Li, D.E. Miser, S. Rabiei, R.T. Yadav, M.R. Hajaligol, Appl. Catal. B-Environ. 43 (2003) 151–162.
[58] B. Qiao, J. Zhang, L. Liu, Y. Deng, Appl. Catal. A-Gen. 340 (2008) 220–228.
[59] B. Qiao, L. Liu, J. Zhang, Y. Deng, J. Catal. 261 (2009) 241–244.
[60] B. Qiao, J. Lin, L. Li, A. Wang, J. Liu, T. Zhang, ChemcatChem 6 (2014) 547–554.
[61] J. Lin, A. Wang, B. Qiao, X. Liu, X. Yang, X. Wang, J. Liang, J. Li, J. Liu, T. Zhang, J. Am. Chem. Soc. 135 (2013) 15314–15317.
[62] M.M. Schubert, S. Hackenberg, A.C. van Veen, M. Muhler, V. Plzak, R.J. Behm, J. Catal. 197 (2001) 113–122.
[63] A. Fukuoka, J. -i. Kimura, T. Oshio, Y. Sakamoto, M. Ichikawa, J. Am. Chem. Soc. 129 (2007) 10120–10125.
[64] K. -i. Tanaka, M. Shou, H. He, X. Shi, X. Zhang, J. Phys. Chem. C 113 (2009) 12427–12433.
[65] C.B. Zhang, H. He, K. Tanaka, Appl. Catal. B-Environ. 65 (2006) 37–43.
[66] O. Pozdnyakova, D. Teschner, A. Wootsch, J. Krohnert, B. Steinhauer, H. Sauer, L. Toth, F.C. Jentoft, A. Knop-Gericke, Z. Paal, R. Schlogl, J. Catal. 237 (2006) 1–16.
[67] B.B. Chen, X.B. Zhu, M. Crocker, Y. Wang, C. Shi, Appl. Catal. B-Environ. 154 (2014) 73–81.